PCCP

PAPER

View Article Online
View Journal | View Issue

Cite this: *Phys. Chem. Chem. Phys.*, 2022, **24**, 23357

The carbon chain growth during the onset of CVD graphene formation on γ-Al_2O_3 is promoted by unsaturated CH_2 ends†

Qi Zhao, [a] Masanori Yamamoto, [b] Kaoru Yamazaki, ‡[c] Hirotomo Nishihara, [b] Rachel Crespo-Otero *[a] and Devis Di Tommaso*[a]

Chemical vapor deposition of methane onto a template of alumina (Al_2O_3) nanoparticles is a prominent synthetic strategy of graphene meso-sponge, a new class of nano porous carbon materials consisting of single-layer graphene walls. However, the elementary steps controlling the early stages of graphene growth on Al_2O_3 surfaces are still not well understood. In this study, density functional theory calculations provide insights into the initial stages of graphene growth. We have modelled the mechanism of CH_4 dissociation on the (111), (110), (100), and (001) γ-Al_2O_3 surfaces. Subsequently, we have considered the reaction pathway leading to the formation of a C6 ring. The γ-Al_2O_3(110) and γ-Al_2O_3(100) are both active for CH_4 dissociation, but the (100) surface has higher catalytic activity towards the carbon growth reaction. The overall mechanism involves the formation of the reactive intermediate CH_2* that then can couple to form C_nH_{2n}* (n = 2–6) intermediates with unsaturated CH_2 ends. The formation of these species, which are not bound to the surface-active sites, promotes the sustained carbon growth in a nearly barrierless process. Also, the short distance between terminal carbon atoms leads to strong interactions, which might lead to the high activity between unsaturated CH_2* of the hydrocarbon chain. Analysis of the electron localization and geometries of the carbon chains reveals the formation of C–Al–σ bonds with the chain growing towards the vacuum rather than C–Al–π bonds covering the γ-Al_2O_3(100) surface. This growth behaviour prevents catalyst poisoning during the initial stage of graphene nucleation.

Received 4th April 2022,
Accepted 9th September 2022

DOI: 10.1039/d2cp01554d

rsc.li/pccp

1. Introduction

Graphene, an atomic thick layer of carbon, has been called a 'wonder material' due to its superior properties such as its high charge carrier mobility, high optical transmissivity, high tensile strength, and excellent thermal conductivity.[1–4] Geim and Novoselov first produced graphene by using a mechanical exfoliation technique using Scotch® tape, which provides monolayer and defect-free graphene.[1] However, this method is only applicable to small-area production. A variety of methods have then been developed to produce large-area and high-quality graphene including chemical exfoliation,[1] electrochemical exfoliation,[5,6] chemical synthesis,[7,8] and chemical vapor deposition (CVD).[9,10] Among these techniques, CVD is one of the most promising synthesis methods because it can produce monolayer graphene over a large area.[7,8,11–14]

[a] *Department of Chemistry, Queen Mary University of London, Mile End Road, London E1 4NS, UK. E-mail: r.crespo-otero@qmul.ac.uk, d.ditommaso@qmul.ac.uk*
[b] *Advanced Institute for Materials Research (WPI-AIMR)/Institute of Multidisciplinary Research for Advanced Materials, Tohoku University, 2-1-1 Katahira, Aoba, Sendai 980-8577, Japan*
[c] *Institute for Materials Research, Tohoku University, 2-1-1 Katahira, Aoba, Sendai 980-8577, Japan*

† Electronic supplementary information (ESI) available: See the supplementary material for the bulk cell of γ-Al_2O_3 (Fig. S1); structural models for CH_4 adsorption on γ-Al_2O_3(111), γ-Al_2O_3(110), γ-Al_2O_3(100), and γ-Al_2O_3(001) catalyst surfaces (Fig. S2); the energy diagram of the first two CH_4 dehydrogenation steps on γ-Al_2O_3 different main exposed surfaces (Fig. S3); energy diagram and intermediate structures for C_2H_6 interacting with surface flexible carbon species (Fig. S4); energy diagram and structures of the C_2H_6 dehydrogenation (Fig. S5); Gibbs energy profile of (a) complete CH_4* dehydrogenation and (b) the formation of C_nH_{2n}* (n = 2–6) species *via* CH_2* coupling on the γ-Al_2O_3 (100) surface at an experimental temperature of 1000 K (Fig. S6); structures and bond lengths between carbon end near surface and center sites of (a) C_2H_4*, (b) C_3H_6*, (c) C_4H_8*, (d) C_5H_{10}*, and (e) C_6H_{12}* on the γ-Al_2O_3(100) surface (Fig. S7); the energy profiles and structures for C_6H_{12}* chain ends with CH_3* on the γ-Al_2O_3(100) surface (Fig. S8); the energy profiles and structures for the concerted mechanism and stepwise mechanism dehydrogenation of C_3H_6* and C_6H_{12}* on γ-Al_2O_3 (100) (Fig. S9 and S10); energy diagram and structures for further H behaviour after carbon ring formation (Fig. S11). See DOI: **https://doi.org/10.1039/d2cp01554d**

‡ Present address: RIKEN Center for Advanced Photonics, RIKEN, 2-1 Hirosawa, Wako, Saitama 351-0198, Japan.

Various hydrocarbon feedstocks have been successfully used as carbon sources, ranging from gases such as methane (CH_4)[3,15,16] and ethylene,[17] liquids such as benzene,[18] to solids such as polymethylmethacrylate (PMMA)[19] and amorphous carbon thin films.[20,21] Since it can generate single-layered graphene (SLG), the most popular combination of carbon feedstock and substrates for graphene production is CH_4 on Cu.[22] In addition to Cu, different metal substrates, including Ni,[14,23–26] Ru,[27–29] Ir,[30–32] Co,[33,34] Fe,[35] Au,[36] Rh,[37] Pt,[38,39] and their alloys,[40,41] have been used for CVD synthesis of graphene films. Also, graphene layers can directly grow on insulating substrates such as SiC,[41,42] sapphire,[43] SiO_2,[44,45] and h-BN.[46,47] Previously, Li *et al.*[48,49] provided an atomic picture of the step-by-step nucleation process of graphene growth on the metal Cu (111) surface. This work demonstrated that at the early stages of the CVD process, linear chains form on the Cu surface, followed by Y-type (furcate) carbon species when new carbon atoms absorb on the side of the linear chains. Finally, ring-containing carbon species and graphene islands form spontaneously stepwise.

Recently, oxides of earth abundant catalysts without noble metal supporting like MgO,[50] CaO,[51] and Al_2O_3[52] have been reported as substrates in the synthesis of novel graphene mesosponge (GMS), a new class of mesoporous carbon materials consisting mainly of single-layer graphene walls with a unique set of properties compared to traditional graphene materials: higher surface area, more developed mesopores, higher oxidation resistance,[53,54] higher softness and elasticity, lower bulk modulus, and force-driven reversible liquid–gas phase transition.[55] But until now, there is a lack of an atomistic description of the steps controlling the early stages of graphene nucleation on metal oxides. Hence, a better understanding of the reaction mechanisms is required to modify the catalytic sites and make them more active in the processes involved. These processes include the activation of adsorbed methane (CH_4*), formation of carbon–hydrogen nuclei, and the subsequent edge growth of graphene islands. By combining experiments and density functional theory (DFT), we previously found that oxygen vacancies on the metal oxide surface of γ-Al_2O_3,[56,57] play an influential role in the CH_4* activation. Park *et al.* reported calculations of the graphene nucleation mechanism on γ-Al_2O_3.[57] In this work, the hypothesis was that growth occurs from adsorbed carbon (C*) atoms. Page *et al.*[58] also reported graphene nucleation on γ-Al_2O_3 using a simplified surface model that did not consider hydroxylated surfaces, which we recently demonstrated to be important in experimental conditions.[56]

In this work, we focus on the mechanism of carbon chain growth during the initial stages of graphene formation on hydroxylated models of γ-Al_2O_3 using DFT calculations. CH_4* activation and the early stages of graphene nucleation occur preferentially on the γ-Al_2O_3 (100) surface. In the complete dehydrogenation process from CH_4* to C*, methylene (CH_2*) is the most stable species on the γ-Al_2O_3 surface whilst C* is highly unstable. The CH_2* radical is involved in the CH_4 conversion into various C_nH_{2n}* (n = 2–6) intermediates to form carbon chains on γ-Al_2O_3 (100) during the initial CVD of graphene.

2. Computational details

The "Vienna *ab initio* simulation package" (VASP.5.4.1) was used to conduct spin polarized DFT calculations. The Perdew–Burke–Ernzerhof (PBE) generalized-gradient approximation (GGA) was adopted to describe the exchange and correlation terms,[59] together with the Grimme's-D3 dispersion correction[60] to provide a more accurate description of the ionic induce dipole interaction than standard DFT–GGA methods.[61] A plane-wave basis set was employed within the framework of the projector augmented wave method.[62] The transition states (TSs) for the elementary reactions were located using the climbing image nudged elastic band (CI-NEB) method,[63] setting the convergence criteria at 0.05 eV $Å^{-1}$ during the TS searching.[1] A Monkhorst–Pack k-point grid of (3 × 3 × 1) and a plane-wave cut-off of 450 eV were used throughout calculations. All atoms were relaxed during the structural optimization of γ-Al_2O_3 and reaction intermediates.

Our previous IR experiments showed that isolated hydroxyl (OH) groups (around 3701 cm^{-1}) at the γ-Al_2O_3 surfaces are present even after annealing at 900 °C for 30 min.[56] Therefore, the surface of γ-Al_2O_3 was modelled using a supercell approach with periodic boundary conditions. The coordinates of γ-Al_2O_3 (the $P2_1/m$ space group)[64] were used as the starting geometry to optimise the internal coordinates and cell parameters of the bulk structure of γ-Al_2O_3.[65] The values of the optimized lattice parameters of γ-Al_2O_3 were a = 5.538 Å, b = 8.347 Å, c = 8.024 Å, β = 90.60° and α = β = 90.00° (Fig. S1, ESI†). The partially hydroxylated slabs of γ-Al_2O_3 (100), γ-Al_2O_3 (110), γ-Al_2O_3 (001), and γ-Al_2O_3 (111) surface containing four atomic layers of the oxide and 15 Å vacuum were constructed starting from the optimised bulk structure. All atoms were relaxed during the optimization. The structures of the surfaces are provided in Section S2 of the ESI.† The mechanisms of CH_4 activation and the early stages of graphene nucleation were investigated using the OH-covered γ-Al_2O_3 (111), γ-Al_2O_3 (110) and γ-Al_2O_3 (001) surfaces. These models are shown in Fig. S2 (ESI†). The adsorption energies of CH_4 on the γ-Al_2O_3 surfaces were computed using the following expression:

$$E_{ads} = E(\text{adsorbate}\cdots CH_4) - E(CH_4) - E(\text{slab}) \quad (1)$$

where the first term is the energy of the optimized surface slab with CH_4 adsorbed, the second term is the energy of the isolated optimized adsorbed molecule, and the third term is the energy of the optimized bare surface slab. A negative value of E_{ads} corresponds to an exothermic adsorption process. The free energy differences of the elementary steps were computed according to the following expression:

$$\Delta G = \Delta E_{DFT} + \Delta E_{ZPE} - T\Delta S \quad (2)$$

where ΔE_{DFT} is the total energy difference from the DFT calculations, ΔE_{ZPE} is the zero-point energy (ZPE) correction

from the frequency analysis, and $T\Delta S$ is the entropy contribution in which the T was fixed at the experimental conditions of T = 1000 K.[56]

3. Results and discussion

3.1 Methane activation on γ-Al_2O_3

We report the calculations of the intermediates and transition states of the first two steps of the CH_4* dehydrogenation, CH_4* → CH_3* + H* and CH_3* → CH_2* + H*. The profiles in Fig. 1 show the ability to activate CH_4* depending on the surface of γ-Al_2O_3: (100), (110), (111), and (001). The structures of the intermediates and transitions states on the γ-Al_2O_3 (100) surface are reported in Fig. 2. For the other surfaces, these structures are shown in Fig. S3 of the ESI.†

On γ-Al_2O_3 (100), after the exothermic adsorption of CH_4* (E_{ads} = −0.20 eV), the breakage of the first C–H bond has a barrier of 1.20 eV and a reaction energy of 0.10 eV. The subsequent dehydrogenation of CH_3* has a barrier of 1.32 eV and reaction energy of −0.06 eV. The barriers for the dissociation step CH_4* → CH_3* + H* on the (111), (001), and (110)[57,66] are 1.92 eV, 1.46 eV, and 2.20 eV, respectively (Fig. 1). The subsequent step, CH_3* → CH_2* + H*, on these surfaces requires even higher barriers. Consequently, the first two CH_4* dehydrogenation steps are kinetically favorable on the γ-Al_2O_3 (100) surface. Martínez *et al.* reported that CH_2* leads to spontaneous C–C chain growth.[67] Hence, the ability to promote the CH_3* dehydrogenation step to generate a stable CH_2* species will also denote the catalytic activity towards carbon growth. However, CH_2* will be a trapped species on the (111) surface due to highly exothermic conversion energies depicted in Fig. 1. We have considered the γ-Al_2O_3 (100) surface to investigate the subsequent steps of CH_2* coupling that initiates the graphene growth due to its favorable CH_4 dissociation properties (Fig. 1). Note also that the (111) surface is more unstable than the (100) and (110) surfaces.[68] In addition, the C–H bond activation barrier on the three-coordinated Al site of the γ-Al_2O_3 (110) surface obtained in this work (1.9 eV) is slightly higher than the one reported by Wischert *et al.* (1.6 eV).[69] Such a difference might be mainly related to differences in the surface model and methods adopted, including the OH coverage, surface unit size, the distance between OH and active sites as well as exchange–correlation functional, pseudopotentials used in the calculations. However, the barriers of the CH_4* → CH_3* + H* and CH_3* → CH_2* + H* steps on the (100) surface are 1.0 eV and 1.2 eV, respectively. These barriers are still lower than the value of 1.6 eV reported by Wischert *et al.* for the (110) surface. In this work the conclusion that the first two CH_4* dehydrogenation steps are kinetically favourable on (100) is still significant.

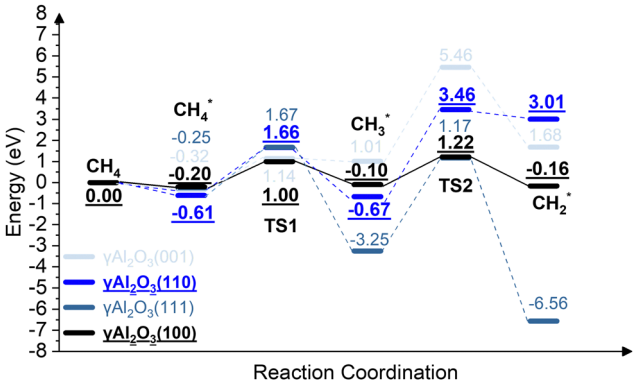

Fig. 1 The energy profiles of the first two steps of the CH_4* dehydrogenation, CH_4* → CH_3* + H* and CH_3* → CH_2* + H*, on the γ-Al_2O_3 (001), γ-Al_2O_3 (111), γ-Al_2O_3 (110), and γ-Al_2O_3 (100) surfaces.

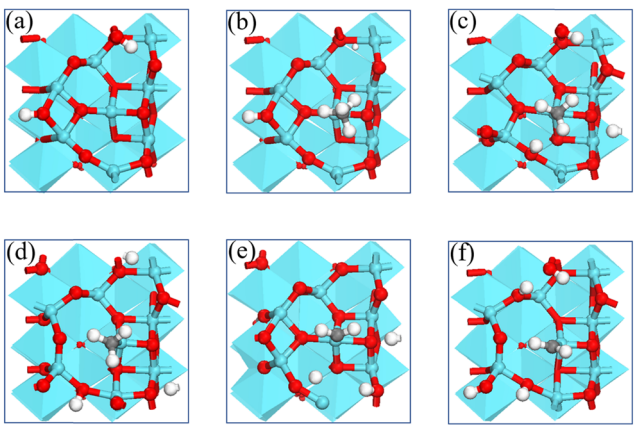

Fig. 2 The structures of intermediates and transition states of the first two CH_4* dehydrogenation steps on the γ-Al_2O_3 (100) surface. (a) Al_2O_3(100); (b) CH_4*; (c) TS1; (d) CH_3*; (e) TS2; (f) CH_2*. (Red, blue, grey, and white spheres represent O, Al, C, and H, respectively).

3.2 Contribution of the (100) and (110) surfaces to CH_2 generation

CH_2 generation on the γ-Al_2O_3 surface is a pseudo-first order reaction on the methane partial pressure.[56] If the entropy contribution is negligible, the activation rate constant k can be approximated with an Eyring-like equation as a function of reaction temperature T,

$$k(T) \sim \frac{k_B T}{h} \exp\left[-\frac{E^*}{k_B T}\right] \quad (3)$$

Table 1 Effective activation energies (E^*) for the generation of CH_2 with the associated rate constants $k(T)$ at T = 900 °C were obtained using eqn (2)

Surface	E^* (eV)	k (s^{-1})
(100)	1.22	1.40×10^8
(110)	3.46	8.74×10^2
Experiment[a]	1.29	7.01×10^7

[a] Rate constant estimated using the experimental barrier.[56]

where k_B and h are the Boltzmann and Planck constants, and E^* represents the effective activation energy experimentally measurable *via* Arrhenius plots.[70] Here, we use the rate constant k to evaluate the contributions of the (100) and (110) surfaces on the CH_4 activation. For the (100) surface, the CH_4 is weakly physisorbed on the surface (E_{ads} (CH_4*) = −0.20 eV) and E^* is calculated as the energy difference between E_{ads} (TS2) and E_{ads} (CH_4). For (110), the CH_4 adsorption energy (E_{ads} (CH_4*) is −0.61 eV) and E^* is the difference between E_{ads} (TS2) and E_{ads} (CH_4*).[67] Table 1 summarizes the effective activation energies and rate constants at T = 900 °C. The value of E^* = 1.22 eV for (100) agrees with the experimental value (1.29 eV). The associated value of k (T = 900 °C) is 1.40×10^8 s^{-1}. For (110), the value of E^* = 3.46 eV is larger and, consequently, the rate is negligibly small (k (T = 900 °C) = 8.74×10^2 s^{-1}). The generation of CH_2 is, therefore, likely to occur on the (100) surface. The hydroxylated surface can generate CH_3, as shown in Fig. 1. However, subsequent dehydrogenation is kinetically unfavorable. Hereafter, we focus on the reactions on the (100) surface.

3.3 Onset of graphene formation: methylene coupling and carbon chain growth

The complete dehydrogenation of CH_4 on γ-Al_2O_3 would lead to the formation of an adsorbed carbon atom (C*). We have computed the energy profile of CH_4 dehydrogenation on γ-Al_2O_3 (100) as a representative surface leading to C*. Fig. 3(a) shows that while the first two dehydrogenation steps CH_4* → CH_3* + H* and CH_3* + H* → CH_2* + 2H* are both favourable, the subsequent steps CH_2* + 2H* → CH* + 3H* and CH* + 3H* → C* + 4H* are endothermic with high activation barriers. But since the pyrolytic carbon deposition of CH_4 occurs at temperatures higher than 800 °C,[56] CH_4 could still dissociate into CH_3*, CH_2*, CH* and C* species on the catalyst surface. To verify the relative stability of these species, we have compared in Fig. 3(b) the binding energies (E_b) of CH_n (n = 0–4) on γ-Al_2O_3 (100). For CH_4*, CH_3*, and CH_2*, the values of E_b are 0.2, 0.6, and 0.5 eV, respectively, but for CH* and C* they are above 4 eV. According to the Sabatier principle, the strong binding of CH* and C* on γ-Al_2O_3 (100) may poison the active centres. Therefore, we propose that the initial CVD growth of graphene on alumina does not involve CH* and C* species. The next steps in the formation of C–C bonds on the γ-Al_2O_3 (100) surface are the coupling reactions $2CH_3$* → C_2H_6* (Fig. 3(c)) and $2CH_2$* → C_2H_4* (Fig. 3(d)). The pathway leading to C_2H_4* in Fig. 3(d) has a lower activation barrier (0.2 eV) compared to C_3H_6* (0.8 eV) in Fig. 3(c). Moreover, the subsequent coupling of CH_3* with the C_2H_6* intermediate is unlikely to occur as the CH_3 ends of the molecule are saturated (the C atom has reached the four coordination), inhibiting further growth as

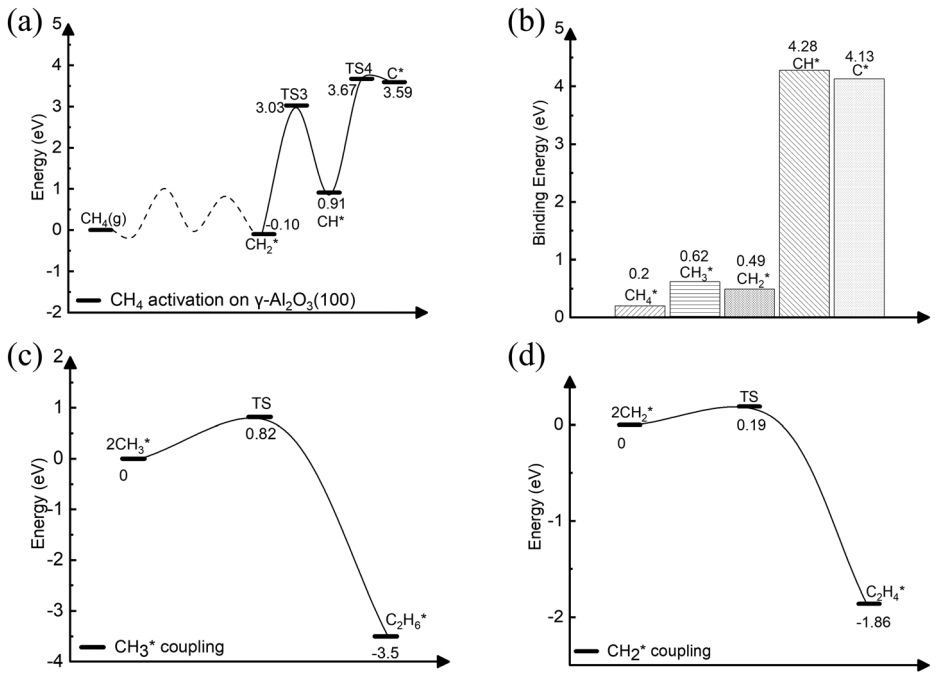

Fig. 3 Energy profiles of the CH_4* dissociation, CH_x* (x = 0–4) binding, and CH_y* (y = 2, 3) coupling reaction on the γ-Al_2O_3 (100) surface. (a) Complete CH_4* dehydrogenation; (b) binding energies of CH_4*, CH_3*, CH_2*, CH* and C; (c) CH_3* coupling; (d) CH_2* coupling. The asterisk (*) denotes a molecule adsorbed on the γ-Al_2O_3 (100) surface.

shown in Fig. S4 of the ESI.† We have also calculated the dehydrogenation of C_2H_6* into C_2H_4* but this process is both kinetically hindered (overall E_a = 4.01 eV) and thermodynamically unfavourable (overall ΔE = 2.05 eV) as shown in Fig. S5 (ESI†). Based on the above results, we conclude that CH_2* is the key intermediate for the subsequent carbon growth steps on the γ-Al_2O_3 (100) surface.

Starting from C_2H_4*, we have considered the methylene coupling processes to form linear C_nH_{2n}* (n = 3–6) species and the C_6H_{12} ring unit, the minimal unit of graphene on γ-Al_2O_3 (100). The energy profile of the chain growth reactions and the corresponding snapshots are shown in Fig. 4 and 5, respectively. Like the CH_2* to C_2H_4* coupling reaction, Fig. 4 shows that the subsequent methylene coupling processes are thermodynamically favourable with each adsorption step, C_nH_{2n} + CH_2(g) → C_nH_{2n} + CH_2*, having negative reaction energies of approximately −2 eV. The formation of the linear species C_2H_4*, C_3H_6*, C_5H_{10}*, and C_6H_{12}* and of the C6 ring have low activation barriers, all well below 1 eV. The exception is the step CH_2* + C_3H_6* → C_4H_8* with an activation energy of 1.87 eV (see Section 3.4 for explanation).

The formation of CH_2* from CH_4 is favourable in entropy but unfavourable in enthalpy on most facets. However, chain growth and cyclization are favourable in enthalpy and unfavourable in entropy. Both factors impact the reaction kinetics and, consequently, how fast the graphene layer grows. To address the role of entropy, we have performed frequency calculations of the reaction intermediates in Fig. 4 involved in C_nH_{2n}* (n = 2–6) species formation *via* CH_2* coupling on the γ-Al_2O_3 (100) surface. The Gibbs free energy diagram confirms that the chain growth is overall a thermodynamically favourable process as well. In the calculation of the reaction barriers, the ZPEs for some systems are non-negligible,[71,72] while in some surface catalytic reactions, adsorption removes many of the degrees of freedom associated with the reaction vacuum, and the ZPE contribution would be negligible relative to the calculated electronic energy.[73] Since our case is similar to the latter, we have neglected ZPE corrections in reaction barrier calculations. These results confirm that the role of unsaturated CH_2* ends for carbon chain growth during the graphene nucleation stage, which makes the initial growth process highly favourable.

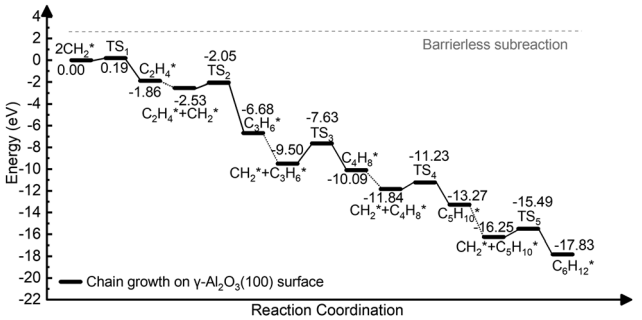

Fig. 4 Energy profile of the formation of C_nH_{2n}* (n = 2–6) species *via* CH_2* coupling on the γ-Al_2O_3 (100) surface.

3.4 The role of unsaturated CH_2 end in promoting graphene growth

To understand the process of CH_2* coupling leading to the carbon chain growth on the γ-Al_2O_3 (100) surface, we have computed the electron localization function (ELF) of the linear C_nH_{2n} (n = 2–6) intermediates. The ELF maps in Fig. 6 represent the electron cloud localized and delocalized around atoms. Using this information, we can determine critical points, chemical bonds, and regions relevant for reactivity (red and orange).

The ELF map for the C_2H_4* structure in Fig. 6(b) shows a localized electron around one end of CH_2* (red area) and a lower electronic charge density distribution around the other end. This weakly saturated CH_2* end allows coupling with free CH_2* on the γ-Al_2O_3 (100) surface making the formation of C_2H_4* highly favorable (Fig. 4). When the longer carbon chains C_4H_8*, C_5H_{10}* and C_6H_{12}* are formed, the sole CH_2* in one position of C_nH_{2n}* is located on the γ-Al_2O_3 (100) surface as shown in Fig. 6(d)–(f). Consequently, the initial growth direction of carbon occurs in the vacuum, away from the surface, and the long carbon species form a C–Al–σ bond with the γ-Al_2O_3 (100) surface rather than grow along the catalytic surface to form a C–Al–π bond. This protects the CVD graphene nucleation reaction sites on γ-Al_2O_3 (100). Otherwise, the accumulation of C_nH_{2n}* species on the surface would poison the catalyst in the early stage by covering these heavy carbon species on the surface. This 'loop' away surface carbon growth mechanism was previously proposed by Zhu *et al.*[74] in the case of Ni clusters.

The ELF analysis can be used to rationalize the high activation energy (1.87 eV) of the CH_2* + C_3H_6* coupling step shown in Fig. 4. The ELF map of C_3H_6* (Fig. 6(c)) shows the high localization of the electron density on both ends of CH_2* ends in C_3H_6* on the catalyst surface. The high barrier is because the two ends of C_3H_6* are bound to the surface-active sites forming highly hindered carbon ends. This is not beneficial for the coupling with the next CH_2*. Therefore, we propose that the carbon chain growth mechanism mostly involves the free CH_2* ends. The work by Lidia Martínez *et al.*[67] also demonstrated that the presence of CH_2 leads to efficient C–C chain growth producing micron-length fibres under metal-catalyst-free gas-phase synthesis. This situation leads to a high barrier for the CH_2* + C_3H_6* → C_4H_8* step (Fig. 4) as both the CH_2* ends have been bonded with surface hindering further reaction. Therefore, unsaturated CH_2* species play a crucial role in promoting the nucleation reaction on γ-Al_2O_3.

The detachment after the carbon chain growth on γ-Al_2O_3(100) can be rationalized because the length between the C_nH_{2n} ends and the active sites on the catalyst surface increases with the chain growth (Fig. S7, ESI†). This is beneficial for the release of the carbon chain as reported by Martínez *et al.*[67] In long carbon chains, the unsaturated CH_2* end would drive sustainable chain growth. There is also a termination pathway that involves the coupling of such open ends with CH_3* species (1.83 eV barrier and −1.79 exothermic reaction energy, as shown in Fig. S8, ESI† depicted). This path would suppress the chain growth as the saturated hydrocarbon will desorb, especially if it occurs at the early stage. Thus, not all reactions will lead to the formation of

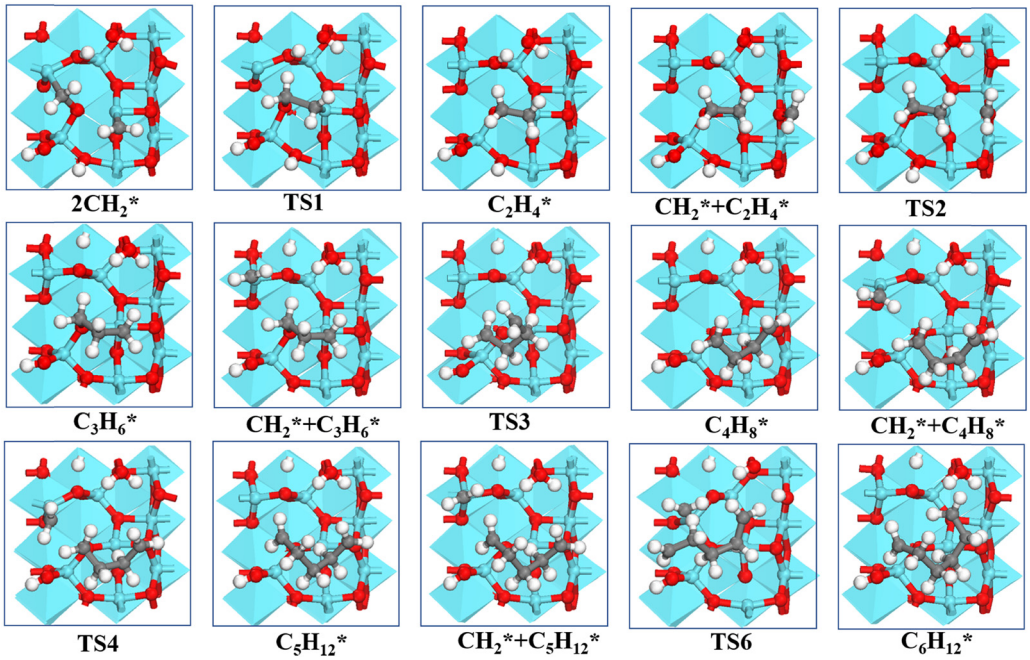

Fig. 5 Structures of the formation of C_nH_{2n}* (n = 2–6) species *via* CH_2* coupling on the γ-Al_2O_3 (100) surface.

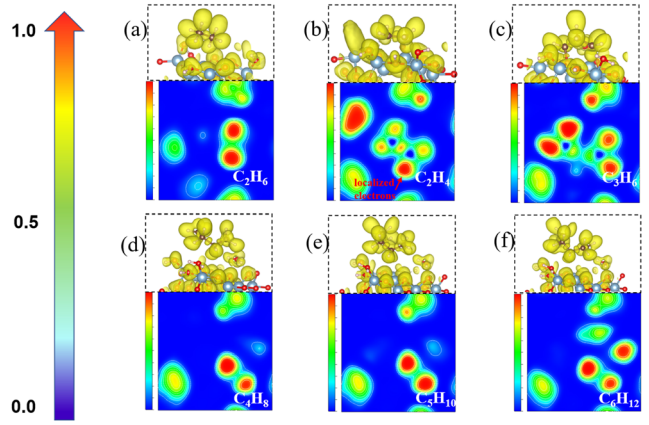

Fig. 6 The electron localization function maps and corresponding side view structures with localized electrons of the C_nH_{2n}* (n = 2–6) species on the γ-Al_2O_3 (100) surface: (a) C_2H_6*; (b) C_2H_4*; (c) C_3H_6*; (d) C_4H_8*; (e) C_5H_{10}*; and (f) C_6H_{12}*. Ongoing from the blue to the red area, there is an increase in the electron density (red areas indicate electron localization).

graphene as there are parallel reactions that form other heavier hydrocarbons which also compete for methane.[56]

The length of the C–C bonds in the C_nH_{2n} species binding on γ-Al_2O_3(100) expands with the chain length (Fig. 7), which could support the carbon units growing away from the γ-Al_2O_3 (100) surface with the formation of C–Al–σ bonds rather than C–Al–π bonds covering the surface.[67] In addition, the C–C length between carbon atoms close to the solid surface is longer than the C–C length of the carbon atoms away from the surface. For instance, the structure of C_6H_{12}* in Fig. 7(g) shows that for the C atoms in the middle positions, C1, C2, C3 and C4, the distances are d(C1–C2) = 1.54 Å, d(C1–C3) = 1.54 Å, d(C2–C4) = 1.54 Å. In comparison, for the terminal C atoms, C5 and C6, d(C4–C6) = 1.49 Å and d(C3–C5) = 1.49 Å. A similar situation can be found in C_4H_8* and C_5H_{10}*. Short bond lengths between terminal carbons correspond to strong interatomic interaction, which might contribute to the high activity among the unsaturated CH_2* of the hydrocarbon chain.

3.5 Dehydrogenation of C_nH_{2n} species and ring condensation

Methylene coupling reaction on γ-Al_2O_3 leading to C_nH_{2n} species is favorable compared to the complete CH_4* dehydrogenation (Fig. 3(a) and 4). Consequently, according to our simulations the species involved in the early stage of graphene growth will contain hydrogen atoms. Previous experimental works showed that metal oxides such as alumina[75] and zirconia[76] can effectively catalyze the dehydrogenation of small alkanes such as propane at high temperatures.

Given the high temperature used in the CVD process, we have computed the dehydrogenation of the intermediates C_3H_6* and C_6H_{12}* with unsaturated CH_2 ends: C_3H_6* to C_3H_4* and C_6H_{12}* to C_6H_{10}*. In a related computational study, Dixit and co-workers investigated the propane dehydrogenation on γ-Al_2O_3 according to two possible surface mechanisms: the concerted and stepwise pathways.[77,78] In the former the olefin formation occurs in a single step, whereas the latter occurs sequential abstraction of hydrogen atoms from the reactant. For the propane molecule, Dixit and co-workers concluded that the concerted pathway was preferred over the stepwise mechanism. As the C_nH_{2n}* intermediates considered in this study (Fig. 5) are not alkanes, as in the work by Dixit and co-workers,[78] but hydrocarbon chains with unsaturated CH_2* ends they will behave differently.

The energy profiles of C_3H_6* and C_6H_{12}* dehydrogenation according to the concerted mechanism are reported in Fig. S9

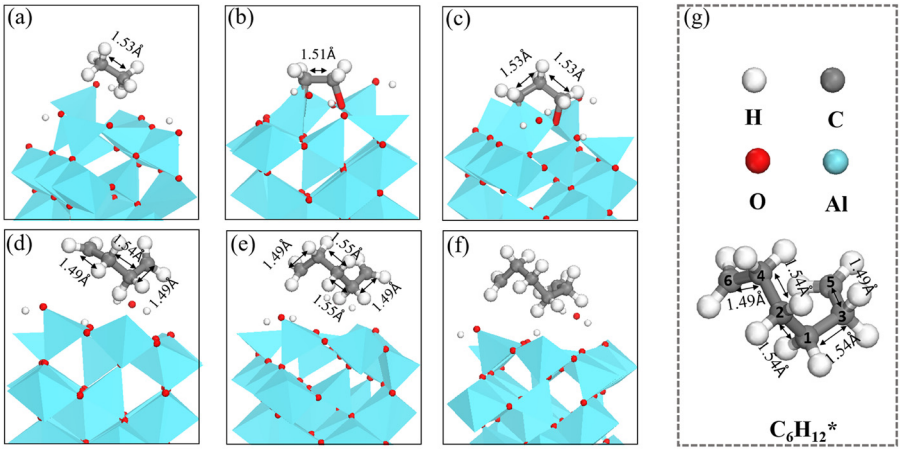

Fig. 7 The structures of (a) C_2H_6*, (b) C_2H_4*, (c) C_3H_6*, (d) C_4H_8*, (e) C_5H_{10}*, (f) and C_6H_{12}* on γ-Al_2O_3(100). (g) Bond lengths in C_6H_{12}*.

of the ESI.† In the concerted pathway, the initial step (C–H activation) involves a six-membered transition state, and the dehydrogenation of C_nH_{2n}* generates two surface-bound hydrogens on the acid–base pair. In the second step (H_2 production), the two surface-bound hydrogen atoms recombine to form molecular hydrogen. For both C_3H_6* and C_6H_{12}* unsaturated intermediates, the dehydrogenation and H_2 formation steps have much higher reaction energies and activation barriers than those reported by Dixit *et al.* for propane on γ-Al_2O_3 (100).[78] The energy profiles of C_3H_6* and C_6H_{12}* dehydrogenation, computed according to the stepwise mechanism, are reported in Fig. S10 of the ESI.† In the stepwise pathway, the initial step (C–H activation) occurs by the abstraction of a proton by a surface oxygen atom followed by a H_2 formation through β-hydrogen elimination[78] elimination. Notwithstanding, the stepwise pathway (Fig. S10, ESI†) is favoured compared to the concerted one (Fig. S9, ESI†), and the stepwise dehydrogenation reactions have much higher activation barriers than the CH_2* coupling reaction in Fig. 4.

The carbon coupling reaction forming a C6 ring was also explored since it represents the early stage of graphene nucleation.[79] As shown in Fig. 8, the ring formation from C_6H_{12}* is energetically favourable (−3.09 eV) and has a low activation barrier (0.34 eV). The calculations suggest that even at the high temperatures at which CVD occurs, the dehydrogenation of the C_2H_{2n} intermediates during initial stage is unlikely because the process is kinetically and thermodynamically unfavourable compared to the ring formation. In addition, as depicted in Fig. S10 (ESI†), the activation barriers of the two elementary dehydrogenation steps of C_3H_6* (4.15 eV and 3.85 eV) are much higher than those of C_6H_{12}* (1.58 eV and 1.96 eV). This could indicate that the dehydrogenation of longer carbon chains could be easier than that of short ones. Thus, in the initial nucleation stage, small-size carbon species may not be stable without hydrogen until they grow to a specific size.

These results indicate that the initial steps of graphene growth involve carbon species that contain hydrogen atoms and confirm that the process does not occur through the

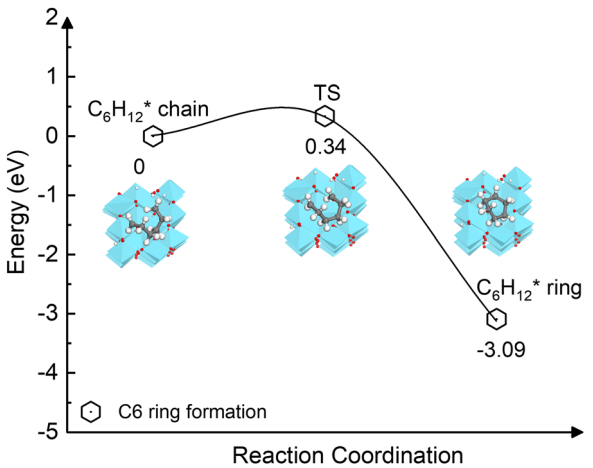

Fig. 8 Energy profile of the ring formation from the carbon chain C_6H_{12}* species on the γ-Al_2O_3 (100) surface.

formation of single carbon. These hydrogen atoms could also hinder the formation of a binding carbon island covering the catalyst surface. Based on these results, an interesting question is when hydrogen-free graphene flake would nucleate. A possible mechanism is that small carbon-containing species are not stable without hydrogen until they grow to a defined size. However, in the early nucleation stage, hydrogen transfer among carbon atoms is much easier than hydrogen desorption from carbon (Fig. S11, ESI†). In perspective, we look forward to answering this question with our future work and understanding the link between hydrogen-free graphene nucleation and hydrocarbon sub-intermediates.

4. Conclusions

This work has reported a systematic investigation of the mechanism of CH_4* dissociation and formation of C_nH_{2n} (n = 2–6) species on γ-Al_2O_3. We found γ-Al_2O_3 (100) to be the most active for the CH_4* dissociation compared with other

low-index surfaces of γ-Al_2O_3. On the (100) surface, methylene coupled to C_2H_4* is kinetically and thermodynamically favoured over the complete CH_4* dehydrogenation to C. Starting from C_2H_4*, we have modelled the formation of linear C_nH_{2n}* (n = 3–6) species and the C_6H_{12} ring unit, which is the fundamental graphene unit. We found that this early carbon chain formation stage before graphene nucleation is nearly barrierless. Electron localization function and structural analyses of carbon chains reveal that the early stages of nucleation involve the formation of C–Al–σ bonds with chains "looping" away from the catalyst surface and the unsaturated CH_2* end remaining active. This is favorable for the initial steps of graphene growth. Our calculations show that hydrogenated carbon species are involved in the early stages of graphene nucleation. These protective bonded hydrogen atoms could weaken the direct C–Al interaction and protect the active sites from carbon covering the γ-Al_2O_3 (100) surface. In summary, our calculations illustrate the first steps of graphene nucleation on γ-Al_2O_3 surfaces and provide insight into the role of active species during the catalytic process.

Author contributions

Qi Zhao, Rachel Crespo-Otero and Devis Di Tommaso conceived and designed the project, and summarized all the ideas provided by co-authors. Qi Zhao conducted the quantum chemistry calculations and wrote the original draft. Hirotomo Nishihara, Masanori Yamamoto, and Kaoru Yamazaki provided valuable comments and suggestions for the original draft. All authors contributed to review and editing.

Conflicts of interest

There are no conflicts to declare.

Acknowledgements

This work was supported by the Cooperative Research Program for CORE lab of "Five-star Alliance", JST SICORP Grant no. JPMJSC2112, Ensemble Grant for Early Career Researchers at Tohoku University, and the UK's Royal Society International Exchanges Cost Share (IEC\R3\193106). Q. Z. thanks the China Scholarship Council for financial support. K. Y. is grateful for the financial support from the Building of Consortia for the Development of Human Resources in Science and Technology funded by MEXT and the Core Research for Evolutional Science and Technology of the Japan Science and Technology Agency (JST CREST, Grant No. JPMJCR16P3). D. D. T. acknowledges the ACT program (Accelerating CCS Technologies, Horizon2020 Project No. 294766), which funded the FUNMIN project. Financial contributions were made from Department for Business, Energy & Industrial Strategy (BEIS) together with extra funding from NERC and EPSRC research councils, United Kingdom, ADEME (FR), MINECO-AEI (ES). We are grateful to the UK Materials and Molecular Model-ling Hub for computational resources, which is partially funded by EPSRC (EP/P020194/1). *Via* our membership of the UK's HEC Materials Chemistry Consortium, which is funded by EPSRC (EP/L000202), this work used the ARCHER UK National Supercomputing Service (**https://www.archer.ac.uk**). This research utilized Queen Mary's Apocrita HPC facility, supported by QMUL Research-IT. **https://doi.org/10.5281/zenodo.438045**.

References

1 K. S. Novoselov, A. K. Geim, S. V. Morozov, D. Jiang, Y. Zhang, S. V. Dubonos, I. V. Grigorieva and A. A. Firsov, *Science*, 2004, **306**, 666–669.
2 A. Balandin, *Nat. Mater.*, 2011, **10**, 569–581.
3 A. A. Balandin, *Nat. Nanotechnol.*, 2010, **5**, 574–578.
4 C. Lee, X. Wei, J. W. Kysar and J. Hone, *Science*, 2008, **321**, 385–388.
5 P. Yu, S. E. Lowe, G. P. Simon and Y. L. Zhong, *Curr. Opin. Colloid Interface Sci.*, 2015, **20**, 329–338.
6 J. Liu, *Graphene-based composites for electrochemical energy storage*, Springer, Singapore, 2017.
7 S. Eigler, M. Enzelberger-Heim, S. Grimm, P. Hofmann, W. Kroener, A. Geworski, C. Dotzer, M. Röckert, J. Xiao and C. Papp, *Adv. Mater.*, 2013, **25**, 3583–3587.
8 S. Stankovich, D. A. Dikin, R. D. Piner, K. A. Kohlhaas, A. Kleinhammes, Y. Jia, Y. Wu, S. T. Nguyen and R. S. Ruoff, *Carbon*, 2007, **45**, 1558–1565.
9 A. Reina, S. Thiele, X. Jia, S. Bhaviripudi, M. S. Dresselhaus, J. A. Schaefer and J. Kong, *Nano Res.*, 2009, **2**, 509–516.
10 X. Li, W. Cai, L. Colombo and R. S. Ruoff, *ACS Nano Lett.*, 2009, **9**, 4268–4272.
11 K. Parvez, S. Yang, X. Feng and K. Müllen, *Synth. Met.*, 2015, **210**, 123–132.
12 Y. Zhang, L. Zhang and C. Zhou, *Acc. Chem. Res.*, 2013, **46**, 2329–2339.
13 M. A. Azam, N. N. Zulkapli, N. Dorah, R. N. A. R. Seman, M. H. Ani, M. S. Sirat, E. Ismail, F. B. Fauzi, M. A. Mohamed and B. Y. Majlis, *ECS J. Solid State Sci. Technol.*, 2017, **6**, M3035–M3048.
14 A. Reina, X. Jia, J. Ho, D. Nezich, H. Son, V. Bulovic, M. S. Dresselhaus and J. Kong, *ACS Nano Lett.*, 2009, **9**, 30–35.
15 X. Li, W. Cai, J. An, S. Kim, J. Nah, D. Yang, R. Piner, A. Velamakanni, I. Jung and E. Tutuc, *Science*, 2009, **324**, 1312–1314.
16 J. K. Wassei, M. Mecklenburg, J. A. Torres, J. D. Fowler, B. Regan, R. B. Kaner and B. Weiller, *Small*, 2012, **8**, 1415–1422.
17 L. Gao, J. R. Guest and N. P. Guisinger, *ACS Nano Lett.*, 2010, **10**, 3512–3516.
18 Z. Li, P. Wu, C. Wang, X. Fan, W. Zhang, X. Zhai, C. Zeng, Z. Li, J. Yang and J. Hou, *ACS Nano*, 2011, **5**, 3385–3390.
19 Z. Sun, Z. Yan, J. Yao, E. Beitler, Y. Zhu and J. M. Tour, *Nature*, 2010, **468**, 549–552.
20 T. Liang, Y. Kong, H. Chen and M. Xu, *Chin. J. Chem.*, 2016, **34**, 32–40.

21 H. Ji, Y. Hao, Y. Ren, M. Charlton, W. H. Lee, Q. Wu, H. Li, Y. Zhu, Y. Wu and R. Piner, *ACS Nano*, 2011, **5**, 7656–7661.
22 P. Wu, W. Zhang, Z. Li and J. Yang, *Small*, 2014, **10**, 2136–2150.
23 M. Xu, D. Fujita, K. Sagisaka, E. Watanabe and N. Hanagata, *ACS Nano*, 2011, **5**, 1522–1528.
24 Q. Yu, J. Lian, S. Siriponglert, H. Li, Y. P. Chen and S. S. Pei, *Appl. Phys. Lett.*, 2008, **93**, 113103.
25 K. S. Kim, Y. Zhao, H. Jang, S. Y. Lee, J. M. Kim, K. S. Kim, J. H. Ahn, P. Kim, J. Y. Choi and B. H. Hong, *Nature*, 2009, **457**, 706–710.
26 J. Lahiri, T. Miller, L. Adamska, I. I. Oleynik and M. Batzill, *ACS Nano Lett.*, 2011, **11**, 518–522.
27 P. W. Sutter, J. I. Flege and E. A. Sutter, *Nat. Mater.*, 2008, **7**, 406–411.
28 E. Loginova, N. C. Bartelt, P. J. Feibelman and K. F. McCarty, *New J. Phys.*, 2008, **10**, 093026.
29 E. Loginova, N. Bartelt, P. Feibelman and K. McCarty, *New J. Phys.*, 2009, **11**, 063046.
30 E. Loginova, S. Nie, K. Thürmer, N. C. Bartelt and K. F. McCarty, *Phys. Rev. B*, 2009, **80**, 085430.
31 J. Coraux, M. Engler, C. Busse, D. Wall, N. Buckanie, F. J. M. Zu Heringdorf, R. Van Gastel, B. Poelsema and T. Michely, *New J. Phys.*, 2009, **11**, 023006.
32 P. Lacovig, M. Pozzo, D. Alfe, P. Vilmercati, A. Baraldi and S. Lizzit, *Phys. Rev. Lett.*, 2009, **103**, 166101.
33 O. Rader, A. Varykhalov, J. Sánchez-Barriga, D. Marchenko, A. Rybkin and A. Shikin, *Phys. Rev. Lett.*, 2009, **102**, 057602.
34 D. Eom, D. Prezzi, K. T. Rim, H. Zhou, M. Lefenfeld, S. Xiao, C. Nuckolls, M. S. Hybertsen, T. F. Heinz and G. W. Flynn, *Nano Lett.*, 2009, **9**, 2844–2848.
35 N. A. Vinogradov, A. A. Zakharov, V. Kocevski, J. Rusz, K. A. Simonov, O. Eriksson, A. Mikkelsen, E. Lundgren, A. S. Vinogradov, N. Mårtensson and A. B. Preobrajenski, *Phys. Rev. Lett.*, 2012, **109**, 026101.
36 S. Nie, N. C. Bartelt, J. M. Wofford, O. D. Dubon, K. F. McCarty and K. Thürmer, *Phys. Rev. B*, 2012, **85**, 205406.
37 E. N. Voloshina, Y. S. Dedkov, S. Torbrügge, A. Thissen and M. Fonin, *Appl. Phys. Lett.*, 2012, **100**, 241606.
38 P. Sutter, J. T. Sadowski and E. Sutter, *Phys. Rev. B*, 2009, **80**, 245411.
39 X. Feng, J. Wu, A. T. Bell and M. Salmeron, *J. Phys. Chem. C*, 2015, **119**, 7124–7129.
40 X. Liu, L. Fu, N. Liu, T. Gao, Y. Zhang, L. Liao and Z. Liu, *J. Phys. Chem. C*, 2011, **115**, 11976–11982.
41 T. Wu, X. Zhang, Q. Yuan, J. Xue, G. Lu, Z. Liu, H. Wang, H. Wang, F. Ding, Q. Yu, X. Xie and M. Jiang, *Nat. Mater.*, 2016, **15**, 43–47.
42 C. Riedl, C. Coletti, T. Iwasaki, A. A. Zakharov and U. Starke, *Phys. Rev. Lett.*, 2009, **103**, 246804.
43 M. K. Jeonghyun Hwang, D. Campbell, H. A. Alsalman, J. Young Kwak, S. Shivaraman, A. R. Woll, A. K. Singh, R. G. Hennig, S. Gorantla, M. H. Rümmeli and M. G. Spencer, *ACS Nano*, 2013, **7**, 385–395.
44 J. Chen, Y. Wen, Y. Guo, B. Wu, L. Huang, Y. Xue, D. Geng, D. Wang, G. Yu and Y. Liu, *J. Am. Chem. Soc.*, 2011, **133**, 17548–17551.
45 H. Bi, S. Sun, F. Huang, X. Xie and M. Jiang, *J. Mater. Chem.*, 2012, **22**, 411–416.
46 J. Xue, J. Sanchez Yamagishi, D. Bulmash, P. Jacquod, A. Deshpande, K. Watanabe, T. Taniguchi, P. Jarillo Herrero and B. J. LeRoy, *Nat. Mater.*, 2011, **10**, 282–285.
47 W. Yang, G. Chen, Z. Shi, C.-C. Liu, L. Zhang, G. Xie, M. Cheng, D. Wang, R. Yang, D. Shi, K. Watanabe, T. Taniguchi, Y. Yao, Y. Zhang and G. Zhang, *Nat. Mater.*, 2013, **12**, 792–797.
48 Y. Li, M. Li, T. Wang, F. Bai and Y. X. Yu, *Phys. Chem. Chem. Phys.*, 2014, **16**, 5213–5220.
49 Y. Li, M. Li, T. Gu, F. Bai, Y. Yu, M. Trevor and Y. Yu, *Appl. Surf. Sci.*, 2013, **284**, 207–213.
50 S. Sunahiro, K. Nomura, S. Goto, K. Kanamaru, R. Tang, M. Yamamoto, T. Yoshii, J. N. Kondo, Q. Zhao, A. Ghulam Nabi, R. Crespo-Otero, D. Di Tommaso, T. Kyotani and H. Nishihara, *J. Mater. Chem. A*, 2021, **9**, 14296–14308.
51 C. Tang, B. Q. Li, Q. Zhang, L. Zhu, H. F. Wang, J. L. Shi and F. Wei, *Adv. Funct. Mater.*, 2016, **26**, 577–585.
52 H. Nishihara, T. Simura, S. Kobayashi, K. Nomura, R. Berenguer, M. Ito, M. Uchimura, H. Iden, K. Arihara, A. Ohma, Y. Hayasaka and T. Kyotani, *Adv. Funct. Mater.*, 2016, **26**, 6418–6427.
53 M. Yamamoto, S. Goto, R. Tang, K. Nomura, Y. Hayasaka, Y. Yoshioka, M. Ito, M. Morooka, H. Nishihara and T. Kyotani, *ACS Appl. Mater. Interfaces*, 2021, **13**, 38613–38622.
54 K. Nomura, H. Nishihara, N. Kobayashi, T. Asada and T. Kyotani, *Energy Environ. Sci.*, 2019, **12**, 1542–1549.
55 K. Nomura, H. Nishihara, M. Yamamoto, A. Gabe, M. Ito, M. Uchimura, Y. Nishina, H. Tanaka, M. T. Miyahara and T. Kyotani, *Nat. Commun.*, 2019, **10**, 2559.
56 M. Yamamoto, Q. Zhao, S. Goto, Y. Gu, T. Toriyama, T. Yamamoto, H. Nishihara, A. Aziz, R. Crespo Otero and D. Di Tommaso, *Chem. Sci.*, 2022, **13**, 3140–3146.
57 J. Park, J. Lee, J. H. Choi, D. K. Hwang and Y. W. Song, *Sci. Rep.*, 2015, **5**, 11839.
58 A. J. Page, S. Saha, H. B. Li, S. Irle and K. Morokuma, *J. Am. Chem. Soc.*, 2015, **137**, 9281–9288.
59 J. P. Perdew, K. Burke and M. Ernzerhof, *Phys. Rev. Lett.*, 1996, **77**, 3865–3868.
60 S. Grimme, J. Antony, S. Ehrlich and H. Krieg, *J. Chem. Phys.*, 2010, **132**, 154104.
61 P. E. Blöchl, *Phys. Rev. B*, 1994, **50**, 17953–17979.
62 G. Kresse and D. Joubert, *Phys. Rev. B*, 1999, **59**, 1758–1775.
63 J. Paier, R. Hirschl, M. Marsman and G. Kresse, *J. Chem. Phys.*, 2005, **122**, 234102.
64 J. Gu, J. Wang and J. Leszczynski, *ACS Omega*, 2018, **3**, 1881–1888.
65 G. Paglia, C. E. Buckley, A. L. Rohl, R. D. Hart, K. Winter, A. J. Studer, B. A. Hunter and J. V. Hanna, *Chem. Mater.*, 2004, **16**, 220–236.
66 M. C. Cholewinski, M. Dixit and G. Mpourmpakis, *ACS Omega*, 2018, **3**, 18242–18250.
67 L. Martínez, P. Merino, G. Santoro, J. I. Martínez, S. Katsanoulis, J. Ault, Á. Mayoral, L. Vázquez, M. Accolla, A. Dazzi, J. Mathurin, F. Borondics, E. Blázquez Blázquez,

N. Shauloff, R. Lebrón Aguilar, J. E. Quintanilla López, R. Jelinek, J. Cernicharo, H. A. Stone, V. A. de la Peña O'Shea, P. L. de Andres, G. Haller, G. J. Ellis and J. A. Martín Gago, *Nat. Commun.*, 2021, **12**, 5937.
68 M. Digne, *J. Catal.*, 2004, **226**, 54–68.
69 R. Wischert, P. Laurent, C. Copéret, F. Delbecq and P. Sautet, *J. Am. Chem. Soc.*, 2012, **134**, 14430–14449.
70 W. Grünert, *Angew. Chem.*, 2012, **51**, 5289.
71 Y. X. Yu, *J. Phys. Chem. C*, 2019, **123**, 205–213.
72 R. Gholizadeh and Y. X. Yu, *Appl. Surf. Sci.*, 2015, **357**, 1187–1195.
73 M. D. Higham, M. G. Quesne and C. R. A. Catlow, *Dalton Trans.*, 2020, **49**, 8478–8497.
74 W. Zhu, A. Börjesson and K. Bolton, *Carbon*, 2010, **48**, 470–478.
75 P. Wang, Z. Xu, T. Wang, Y. Yue, X. Bao and H. Zhu, *Catal. Sci. Technol.*, 2020, **10**, 3537–3541.
76 Y. Zhang, Y. Zhao, T. Otroshchenko, H. Lund, M.-M. Pohl, U. Rodemerck, D. Linke, H. Jiao, G. Jiang and E. V. Kondratenko, *Nat. Commun.*, 2018, **9**, 1–10.
77 J. Joubert, F. Delbecq and P. Sautet, *J. Catal.*, 2007, **251**, 507–513.
78 M. Dixit, P. Kostetskyy and G. Mpourmpakis, *ACS Catal.*, 2018, **8**, 11570–11578.
79 W. Zhang, P. Wu, Z. Li and J. Yang, *J. Phys. Chem. C*, 2011, **115**, 17782–17787.

